

Unsteady mixed convection flow of variable viscosity nanofluid in a micro-channel filled with a porous medium

B Hindebu^{1*}, O D Makinde² and L Guta³

¹Department of Applied Mathematics, Adama Science and Technology University, Adama, Ethiopia

²Faculty of Military Science, Stellenbosch University, Private Bag X2, Saldanha 7395, South Africa

³Department of Applied Mathematics, Adama Science and Technology University, Adama, Ethiopia

Received: 23 June 2020 / Accepted: 13 April 2021 / Published online: 16 May 2021

Abstract: Nanofluids flow and heat transfer in micro-channels have a wide range of attributes in industrial process as well as engineering and biomedical applications. Therefore, the aim of this study is to analyze the hydrodynamic and thermal behaviors of unsteady mixed convection flow of nanofluid in a micro-channel filled with a saturated porous medium. The highly nonlinear governing partial differential equations corresponding to the momentum, energy and concentration profiles were formulated and solved numerically by utilizing the semi-discretization finite difference method. The effects of each governing thermophysical parameters on the micro-channel hydrodynamic and thermal behaviors are discussed with the usage of graphs. The numerical results indicate that the velocity and temperature profiles show an increasing behavior with pressure gradient parameter, variable viscosity parameter, Eckert number, thermal Grashof number, solutal Grashof number and thermophoresis parameter, whereas the concentration profile increases with increasing values of suction/injection Reynolds number, porous medium shape parameter, Forchheimer number, Prandtl number, Schmidt number and thermophoresis parameter. Moreover, the result reveals that the skin friction coefficient, the Nusselt number and the Sherwood number are higher for large values of pressure gradient parameter, thermal Grashof number, Prandtl number and Schmidt number.

Keywords: Micro-channel; Nanofluids; Variable viscosity; Suction/injection; Porous medium

1. Introduction

Nowadays, heat transfer enhancement and thermal efficiency are becoming important engineering topics related to conservation of the limited energy and enhancing thermodynamic performance [1]. As a result, for the last four to five decades, many technologies have been presented to improve the efficiency in different heat conversion devices or heat exchangers. Among the technological revolutions, micro-channels have been identified as the most essential one to transport fluids in a miniaturization systems [2]. The concept of micro-channels was demonstrated by Tuckerman and Pease [3] for the first time. After the groundbreaking work of Tuckerman and Pease, micro-channels have been used in a wide range of industrial and engineering applications including electronic cooling, cooling

of computer chips, automotive heat exchangers, laser equipment, aerospace technology, heat sinks of MEMS-based devices, drug delivery applications, DNA hybridization, environmental control, pharmaceutical and biotechnological applications [4–6].

In recent years, a number of research studies have been communicated comprising the analysis of fluid flow and heat transfer phenomena in micro-channels. To mention few, Reddy et al. [7] investigated the combined effects of wall slip, viscous dissipation and Joule heating on MHD electro-osmotic peristaltic motion of Casson fluid through a rotating asymmetric micro-channel. Meanwhile, the explanation of the influence of slim obstacle geometry on the flow and heat transfer in micro-channels was given by Kmiotek and Kucab-Pietal [8]. Moreover, similar studies can be found in the literature [9–11].

Despite of their high heat transfer capabilities, a challenging problem in micro-channels is that the higher convection heat transfer coefficient comes at the cost of greater

*Corresponding author, E-mail: hindebubu@gmail.com

pressure drop per unit length and hence there is a greater requirement of pumping power in the micro-channel flow geometries [12]. Besides, common heat transfer fluids or base fluids such as water, oils and ethylene are poor in heat transfer capabilities due to their low thermal conductivity [13]. Because of the aforementioned reasons, novel technologies with the potential of improving the fluid transport properties such as thermal conductivity of the working fluid are of great interest for flows in micro-channels once again. From this perspective, utilization of nanofluids in micro-channels is among the convection heat transfer augmentation techniques. The term nanofluid was first pioneered by Choi [14] in 1995 to indicate that nanofluids are engineered suspension or dispersion of nanometer-sized particles (1–100 nm) into the common base fluids. Nanofluids have higher thermal conductivity, better absorption capacity and wonderful stability [15].

The usage of nanofluids in micro-channels has large-scale utilization particularly as coolants in industrial and technological processes such as electronics cooling, transportation (engine cooling/vehicle thermal management), space and nuclear system cooling, defense applications (cooling military devices and systems), cooling in chillers and refrigerators, cancer therapy, air conditioning, CPU, MEMS and drug delivery applications [16, 17]. Consequently, there are many researchers, for instance, [18–23] who were reported their research works in line with nanofluids flow and heat transfer phenomena in micro-channels.

Another attractive technique for improving the convection heat transfer characteristics is the usage of porous media in micro-channels and heat exchangers. According to [24], a porous medium is a solid matrix which is characterized by the presence of void spaces called pores which are interconnected by a network of channels where a fluid can move. Fluid flow and heat transfer in channels filled with porous media occur in a numerous areas of applications including storage of radioactive nuclear waste, transpiration cooling, filtration, geothermal extraction, crude oil extraction, heating and cooling in buildings, systems, underground water movement, biomedical sciences and so on [24–26]. For the first time in 1856, Henry Darcy developed the basic law known as Darcy's law that governs the flow of fluids through a porous media on the basis of experimental results for the flow of water through beds of sand [27]. Following the work of Darcy, the analysis of fluid flow in micro-channels filled with porous media has been receiving prodigious interests by many researchers including [28–32].

From the above discussion, it can be ascertained that the analysis of nanofluid flow and heat transfer phenomena in micro-channels was presented by a number of researchers. However, many of such studies were modeled through a

single phase flow model by neglecting the slip velocity between the particle and base fluid. Hence, more investigations of nanofluids as a two-phase flow which is also known as the Buongiorno model [33] should be considered because the slip velocity between the particle and base fluid plays important role on the heat transfer performance of nanofluids particularly from the industrial applications point of view. There are few research articles in which the Buongiorno model was utilized to study nanofluids flow and heat transfer in micro-channels. Such studies are even scarce in the presence of porous media.

Therefore, this paper is the first attempt in employing the two-phase model for studying nanofluid flow and heat transfer in a micro-channel filled with a porous medium. For fluid flow in micro-channels, there always exists high frictional resistance of the coolants leading to generation of high temperature within the fluid, and thus, the viscosity of the fluid is assumed to be erratic with temperature [34]. Thus, this study mainly focused on the mathematical investigation of unsteady flow of variable viscosity nanofluid through a micro-channel filled with a saturated porous medium together with heat transfer characteristics due to mixed convection.

2. Mathematical model formulation

We consider unsteady mixed convective flow of Newtonian nanofluid in a micro-channel filled with a saturated porous medium. The micro-channel is assumed to have permeable walls placed at $y = 0$ and $y = a$ as shown in Fig. 1, where a denotes the distance between the two walls.

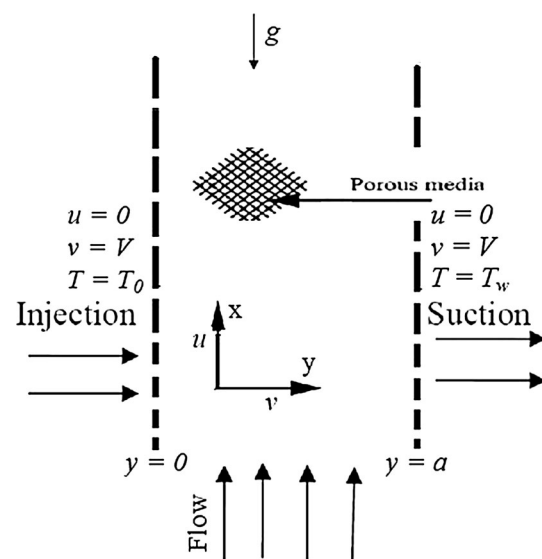


Fig. 1 Physical flow model and coordinate system

It is also assumed that the flow is driven by the combined actions of axial pressure gradient together with fluid body forces due to solutal and thermal buoyancy variations. Furthermore, a nanofluid injection into the micro-channel takes place through the left wall ($y = 0$), while a nanofluid suction out of the micro-channel occurs at the right wall ($y = a$). At time $t = 0$, the fluid temperature is maintained at T_0 and the fluid is in the static position. For large time ($t > 0$), the flow occurs only when the nanofluid starts to move with the time within the micro-channel flow regime and is subjective to a convective heat exchange with the surrounding boundaries. We also impose no-slip conditions for axial velocity at the walls, and the wall temperature is taken to be non-uniform where the left micro-channel wall is placed at temperature T_0 , while the right wall is placed at temperature T_1 such that $T_0 < T_1$. Both the temperature and concentration are initially zero within the fluid except at the walls where the constant values are maintained.

The nanofluid dynamic viscosity is assumed to be an exponential decreasing function of temperature and hence given as $\mu(T) = \mu_0 e^{-\gamma(T-T_0)}$ where γ is a viscosity variation parameter and μ_0 is the dynamic viscosity at the left wall of the micro-channel. The axial convection terms are also assumed to be very small in the model equations and are neglected as compared to the normal convection terms, and thus, we have $\frac{\partial T}{\partial x} \ll \frac{\partial T}{\partial y}$, $\frac{\partial C}{\partial x} \ll \frac{\partial C}{\partial y}$, $\frac{\partial u}{\partial x} \ll \frac{\partial u}{\partial y}$.

Therefore, by considering the above assumptions and using the Darcy–Forchheimer flow model, the governing equations of continuity, linear momentum, energy and concentration under the usual Oberbeck–Boussinesq approximation are presented in the following form.

$$\frac{\partial u}{\partial x} = 0 \tag{1}$$

$$\frac{\partial u}{\partial t} + V \frac{\partial u}{\partial y} = -\frac{1}{\rho} \frac{\partial P}{\partial x} + \frac{1}{\rho} \frac{\partial}{\partial y} \left[\mu(T) \frac{\partial u}{\partial y} \right] - \frac{\mu(T)u}{\rho K} - \frac{bu^2}{\sqrt{K}} + \beta_1 g(T - T_0) + \beta_2 g(C - C_0) \tag{2}$$

$$\frac{\partial T}{\partial t} + V \frac{\partial T}{\partial y} = \alpha \frac{\partial^2 T}{\partial y^2} + \Gamma \left[D_B \frac{\partial C}{\partial y} \frac{\partial T}{\partial y} + \frac{D_T}{T_0} \left(\frac{\partial T}{\partial y} \right)^2 \right] + \frac{\mu(T)}{\rho C_p} \left(\frac{\partial u}{\partial y} \right)^2 + \frac{\mu(T)u^2}{\rho C_p K} + \frac{bu^3}{C_p \sqrt{K}} \tag{3}$$

$$\frac{\partial C}{\partial t} + V \frac{\partial C}{\partial y} = D_B \frac{\partial^2 C}{\partial y^2} + \frac{D_T}{T_0} \frac{\partial^2 T}{\partial y^2} \tag{4}$$

with the initial and boundary conditions:

$$\left. \begin{aligned} u(y, 0) = 0, T(y, 0) = T_0, C(y, 0) \\ u(0, t) = 0, T(0, t) = T_0, \\ = C_0 \text{ and } \left. \begin{aligned} D_B \frac{\partial C(0,t)}{\partial y} = -\frac{D_T}{T_0} \frac{\partial T(0,t)}{\partial y}, \\ u(a, t) = 0, T(a, t) = T_1, \\ C(a, t) = C_1 \end{aligned} \right\} \text{ for } t > 0 \end{aligned} \right\} \tag{5}$$

where u is the axial velocity, V is constant wall suction/injection velocity, a is the micro-channel width, ρ is the nanofluid density, P is nanofluid pressure, T is the nanofluid temperature, C is the nanoparticles concentration, C_p is specific heat at constant pressure, and α is the thermal diffusivity of the nanofluid defined as $\alpha = \frac{k}{\rho C_p}$ where k is thermal conductivity of the nanofluid, Γ is the heat capacity ratio which is the ratio of heat capacity of the nanoparticle and heat capacity of base fluid, K is the porous media permeability, g is gravitational acceleration, D_B is the Brownian diffusion coefficient, D_T is thermal diffusion coefficient, γ is the viscosity variation parameter, and b is the second-order dimensionless (porous inertia) resistance coefficient also known as the dimensionless Forchheimer constant such that $b = 0$ corresponds to the Darcy law.

3. Non-dimensional formulation

In order to non-dimensionalize the above governing equations, we introduce the following dimensionless variables.

$$\left. \begin{aligned} \eta = \frac{y}{a}, X = \frac{x}{a}, W = \frac{\rho a u}{\mu_0}, \tau = \frac{\mu_0 t}{\rho a^2}, \theta = \frac{T - T_0}{T_1 - T_0}, \\ \phi = \frac{C - C_0}{C_1 - C_0}, P^* = \frac{\rho a^2 P}{\mu_0^2}, \\ A = -\frac{\partial P^*}{\partial X}, \text{Re} = \frac{\rho V a}{\mu_0}, \lambda = \gamma(T_1 - T_0), \\ \text{Da} = \frac{K}{a^2}, S = \frac{a^2}{K}, F = \frac{ba}{\rho \sqrt{K}}, \\ \text{Gt} = \frac{\beta_1 g \rho^2 a^3 (T_1 - T_0)}{\mu_0^2}, \text{Gc} = \frac{\beta_2 g \rho^2 a^3 (C_1 - C_0)}{\mu_0^2}, \\ \text{Nt} = \Gamma \frac{D_T}{T_0} (T_1 - T_0) \frac{\rho}{\mu_0}, \\ \text{Nb} = \Gamma D_B (C_1 - C_0) \frac{\rho}{\mu_0}, \text{Ec} = \frac{\mu_0^2}{\rho^2 a^2 C_p (T_1 - T_0)}, \\ \text{Pr} = \frac{\mu_0}{\rho \alpha}, \text{Sc} = \frac{\mu_0}{\rho D_B} \end{aligned} \right\} \tag{6}$$

Using the above dimensionless variables, Eqs. (1)–(5) take the following form.

$$\frac{\partial W}{\partial X} = 0 \quad (7)$$

$$\frac{\partial W}{\partial \tau} + \text{Re} \frac{\partial W}{\partial \eta} = A + e^{-\lambda \theta} \left[\frac{\partial^2 W}{\partial \eta^2} - \lambda \frac{\partial \theta}{\partial \eta} \frac{\partial W}{\partial \eta} \right] - e^{-\lambda \theta} S^2 W - F W^2 + \text{Gt} \theta + \text{Gc} \phi \quad (8)$$

$$\frac{\partial \theta}{\partial \tau} + \text{Re} \frac{\partial \theta}{\partial \eta} = \frac{1}{\text{Pr}} \frac{\partial^2 \theta}{\partial \eta^2} + \text{Nb} \frac{\partial \phi}{\partial \eta} \frac{\partial \theta}{\partial \eta} + \text{Nt} \left(\frac{\partial \theta}{\partial \eta} \right)^2 + \text{Ece}^{-\lambda \theta} \left(\frac{\partial W}{\partial \eta} \right)^2 + S^2 \text{Ece}^{-\lambda \theta} W^2 + F \text{Ec} W^3 \quad (9)$$

$$\frac{\partial \phi}{\partial \tau} + \text{Re} \frac{\partial \phi}{\partial \eta} = \frac{1}{\text{Sc}} \left[\frac{\partial^2 \phi}{\partial \eta^2} + \frac{\text{Nt}}{\text{Nb}} \frac{\partial^2 \theta}{\partial \eta^2} \right] \quad (10)$$

with the initial and boundary conditions:

$$\left. \begin{aligned} W(\eta, 0) = 0, \theta(\eta, 0) = 0, \phi(\eta, 0) = 0 \\ W(0, \tau) = 0, \theta(0, \tau) = 0, \\ \text{Nb} \frac{\partial \phi(0, \tau)}{\partial \eta} + \text{Nt} \frac{\partial \theta(0, \tau)}{\partial \eta} = 0, \\ W(1, \tau) = 0, \theta(1, \tau) = 1, \\ \phi(1, \tau) = 1 \end{aligned} \right\} \text{for } \tau > 0 \quad (11)$$

where τ is dimensionless time, Re is the suction/injection Reynolds number, Gt is the Grashof number due to thermal buoyancy effect, Gc is the Grashof number due to solutal buoyancy effect, Ec is the Eckert number, Pr is the Prandtl number, A is dimensionless axial pressure gradient parameter, λ is the dimensionless viscosity variation parameter, S is the porous media shape factor parameter, F is the Forchheimer number also called the Forchheimer inertial resistance which is the second-order porous media resistance parameter, Sc is the Schmidt number, Nb is the Brownian motion parameter, and Nt is the thermophoresis parameter.

Other physical quantities of practical significance in this study are the skin friction coefficient C_f , the local Nusselt number Nu and the local Sherwood number Sh. In the study of flow and thermal systems, it is mandatory to examine the influences of the thermophysical parameters on C_f , Nu and Sh. This is because the consequences of excessive heat generation are not only evaluated from the economy perspectives like the efficient operation of machinery, property destruction, etc., but also it may jeopardize the lives of machine operating personnel. Therefore, the dimensionless skin friction coefficient C_f , local Nusselt number Nu and local Sherwood number Sh at the micro-channel walls are given as follows.

$$\left. \begin{aligned} C_f = e^{-\lambda \theta} \frac{dW}{d\eta} \Big|_{\eta=0,1}, \\ \text{Nu} = - \frac{d\theta}{d\eta} \Big|_{\eta=0,1}, \text{Sh} = - \frac{d\phi}{d\eta} \Big|_{\eta=0,1} \end{aligned} \right\} \quad (12)$$

4. Numerical method

The semi-discretization finite difference scheme also known as the numerical method of lines (MOL) which is basically proceeded in two steps, namely the space discretization and the time integration, was applied to solve the governing Eqs. (8)–(10) with initial and boundary conditions (11). This version is also known as the vertical method of lines which is discrete in space and continuous in time. In the space discretization, the spatial derivatives are first approximated using finite difference method in such a way that the partial differential equations (PDEs) are transformed into a system of ordinary differential equations (ODEs) corresponding to the solution at some grid points as a function of time.

The discretization of the governing equations is based on a linear Cartesian mesh and uniform grid on which finite differences are taken. Both the second and first spatial derivatives are approximated by second-order central differences. The equations corresponding to the first and last grid points are modified to incorporate the boundary conditions. The resulting nonlinear system of the initial value ODEs problem is then solved iteratively using the integrator Maplesoft-dsolve in Maple. Thus, the semi-discretization scheme for the velocity, temperature and concentration fields is recorded as follows.

$$\begin{aligned} \frac{dW_i}{d\tau} = & A - \text{Re} \frac{W_{i+1} - W_{i-1}}{2\Delta\eta} \\ & - e^{-\lambda \theta_i} S W_i - F W_i^2 + \text{Gt} \theta_i + \text{Gc} \phi_i \\ & + e^{-\lambda \theta_i} \left[\frac{W_{i-1} - 2W_i + W_{i+1}}{(\Delta\eta)^2} - \lambda \frac{\theta_{i+1} - \theta_{i-1}}{2\Delta\eta} \right. \\ & \left. \cdot \frac{W_{i+1} - W_{i-1}}{2\Delta\eta} \right] \end{aligned} \quad (13)$$

$$\begin{aligned} \frac{d\theta_i}{d\tau} = & -\text{Re} \frac{\theta_{i+1} - \theta_{i-1}}{2\Delta\eta} + \frac{1}{\text{Pr}} \frac{\theta_{i-1} - 2\theta_i + \theta_{i+1}}{(\Delta\eta)^2} \\ & + \text{Nb} \frac{\phi_{i+1} - \phi_{i-1}}{2\Delta\eta} \cdot \frac{\theta_{i+1} - \theta_{i-1}}{2\Delta\eta} \\ & + \text{Nt} \left[\frac{\theta_{i+1} - \theta_{i-1}}{2\Delta\eta} \right]^2 + \text{Ece}^{-\lambda \theta_i} \left[\frac{W_{i+1} - W_{i-1}}{2\Delta\eta} \right]^2 \\ & + S^2 \text{Ec} W_i^2 + S \text{Ec} W_i^3 \end{aligned} \quad (14)$$

$$\frac{d\phi_i}{d\tau} = -Re \frac{\phi_{i+1} - \phi_{i-1}}{2\Delta\eta} + \frac{1}{Sc} \left[\frac{\phi_{i-1} - 2\phi_i + \phi_{i+1}}{(\Delta\eta)^2} + \frac{Nt}{Nb} \cdot \frac{\theta_{i-1} - 2\theta_i + \theta_{i+1}}{(\Delta\eta)^2} \right] \quad (15)$$

with initial conditions

$$W_i(0) = 0, \quad \theta_i(0) = 0, \quad \phi_i(0) = 0 \quad (16)$$

where $W_i(\tau) = W(\eta_i, \tau)$, $\theta_i(\tau) = \theta(\eta_i, \tau)$, $\phi_i(\tau) = \phi(\eta_i, \tau)$ and the spatial interval $[0, 1]$ is partitioned into N equal subintervals. The grid size and the grid points are defined as $\Delta\eta = \frac{1}{N}$ and $\eta_i = \frac{i-1}{\Delta\eta}$ for $1 \leq i \leq N + 1$.

5. Results and discussion

5.1. Transient and steady-state profiles

The transient and steady-state profiles for the velocity, temperature and concentration are portrayed in Figs. 2(a), (b) and 3. From these figures, it can be observed that the velocity, temperature and concentration profiles show a parabolic shape with transient increase and reach the steady states at about $\tau \geq 0.9$. Besides, Fig. 2(a) indicates that the velocity profile attains its maximum value around the micro-channel center line region and then reduces to zero because of the no-slip boundary conditions. Figure 2(b) demonstrates that the temperature profile attained its lowest value at the left wall and gradually increasing toward the right wall where it attained its pick value, whereas Fig. 3 shows that the concentration profile attained its pick value at the left wall and starts decreasing gradually toward the right wall where it attains its lowest value.

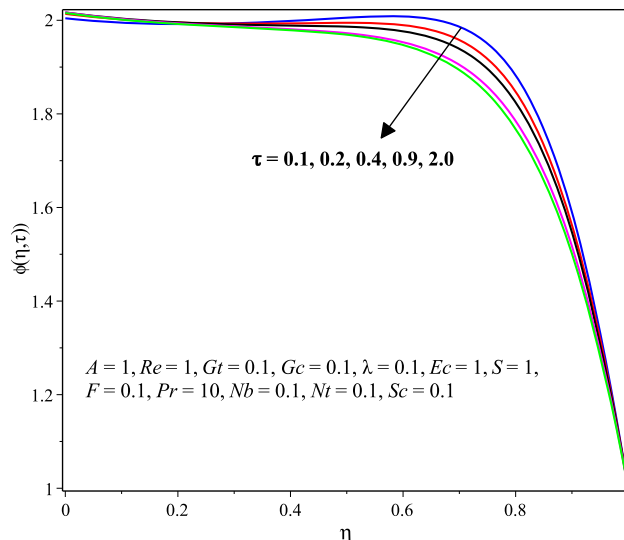


Fig. 3 Transient and steady-state solution of concentration profile

5.2. Parameter dependency of solutions

Figures 4(a), 4(b) and 5 are double graphs that portray the effects of Re and A on the fluid velocity, temperature and concentration profiles. In the current study, we considered that there is a uniform fluid injection into the flow regime at the left permeable wall (vertical line $\eta = 0$) and suction out at the right wall (vertical line $\eta = 1$). Figure 4(a) and 4(b) portrays that as the values of the suction/injection Reynolds number Re increase, both the velocity and temperature profiles tend to decline and also, it can be seen that the velocity profile shows slightly skewing behavior toward the left wall of the micro-channel. This result is similar to the one obtained by Rundora and Makinde [35]. Indeed, the argument for this result may be ascribed to the fact that as a

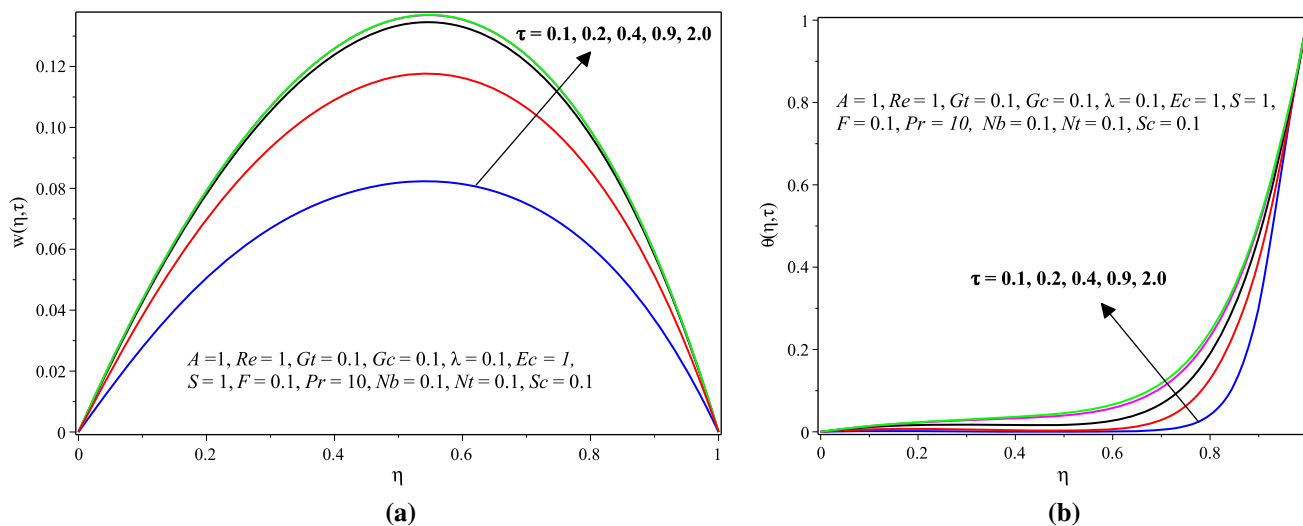


Fig. 2 (a) Velocity and (b) temperature profiles with transient and steady-state solutions

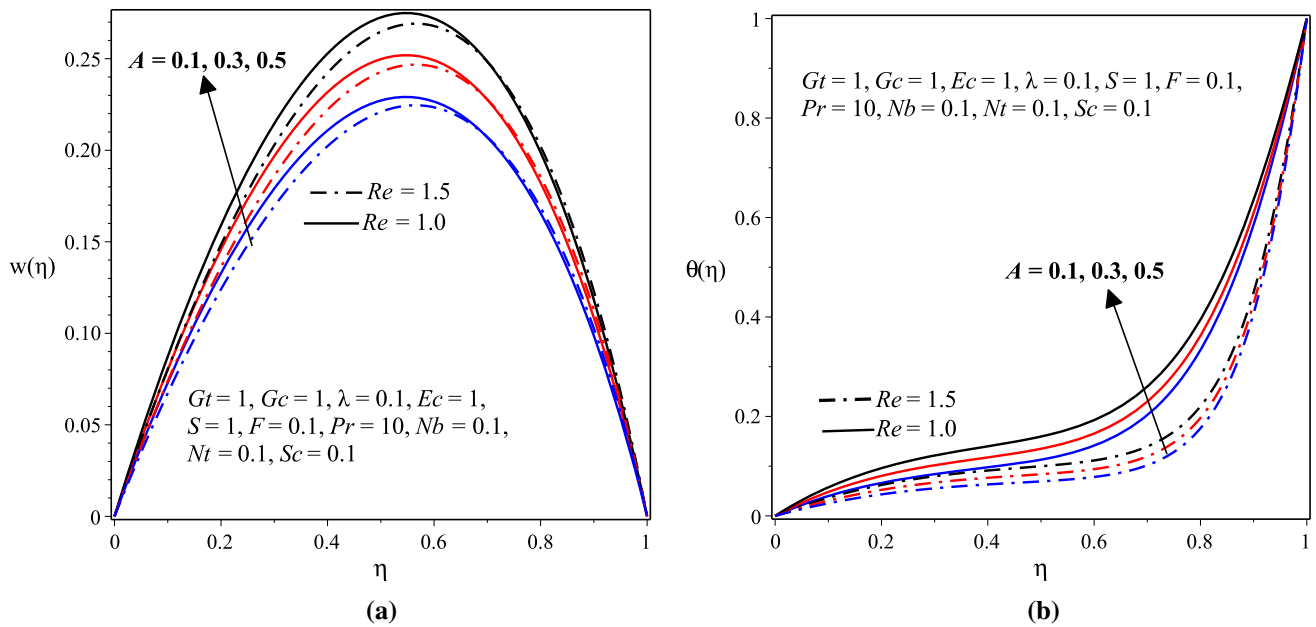


Fig. 4 (a) Velocity and (b) temperature profiles with varying A and Re

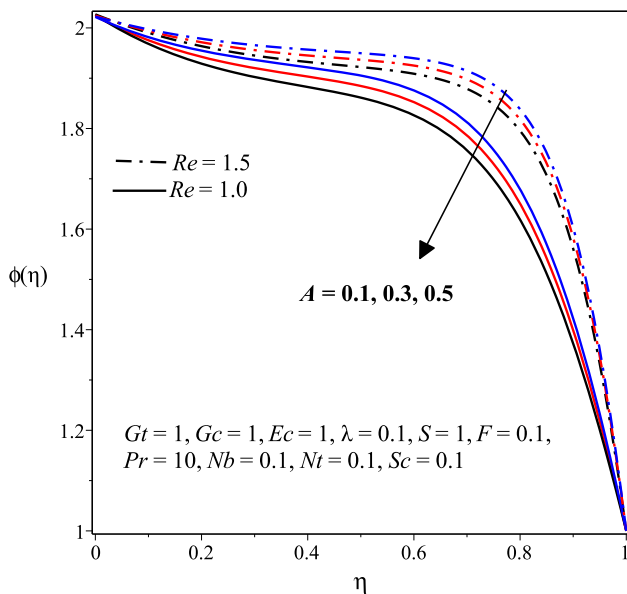


Fig. 5 Effects of A and Re on concentration profile

fluid is sucked out of the right wall, the velocity toward the right wall is higher than elsewhere in the micro-channel and this in turn increases the rate of convective heat transfer out of the right wall resulting in a significant drop in fluid temperature.

Figure 4(a) and 4(b) also reveals that both the fluid velocity and temperature profiles increase as the pressure gradient parameter A increases. This is the case because the fluid motion is due to the pressure gradient, and hence, as A increases, the fluid moves faster which in turn increases the fluid velocity and temperature. Re and A have shown

the opposite effects on the concentration profile as depicted in Fig. 5.

Figures 6(a), 6(b) and 7 display the effects of the thermal Grashof number Gt and the solutal Grashof number Gc on velocity, temperature and concentration profiles. The velocity and temperature profiles increase with Gt and Gc as shown in Fig. 6(a) and 6(b). This is the case because as the values of Gt and Gc enhanced, the body forces acting on the fluid (thermal and solutal buoyancy forces) also get enhanced which also enhance the velocity that in turn increases the viscous heating and hence increases the fluid temperature. The opposite scenario is demonstrated in Fig. 7 for the concentration profile due to the fact that a small temperature increment will cause a very small decrement in concentration which is also known as the cross-diffusion effect.

Figure 8(a) and 8(b) pictures that as the dimensionless variable viscosity parameter λ increases, a significant rise in the fluid velocity and temperature profiles is observed. This is the case because an increase in λ reduces the fluid viscosity since $\mu(T) = \mu_0 e^{-\lambda\theta}$. So, the fluid becomes less viscous, and hence, friction between fluid layers decreases due to which fluid velocity remains at higher levels for higher values of λ . Rundora and Makinde [35] reported a similar result. However, increasing the values of λ decreases the concentration profile as indicated in Fig. 10(a).

The effects of the Eckert number Ec on the fluid velocity, temperature and concentration profiles are depicted in Figs. 9(a), 9(b) and 10(a), respectively. From Fig. 9(a) and 9(b), it is observed that as the magnitude of

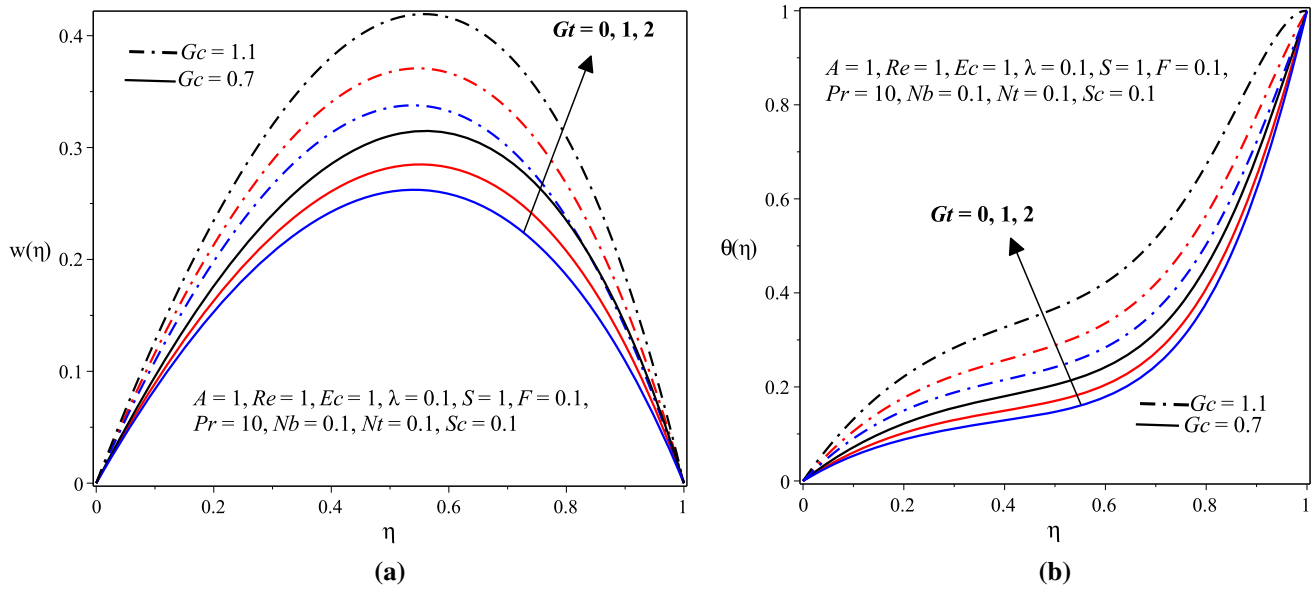


Fig. 6 (a) Velocity and (b) temperature profiles with varying Gt and Gc

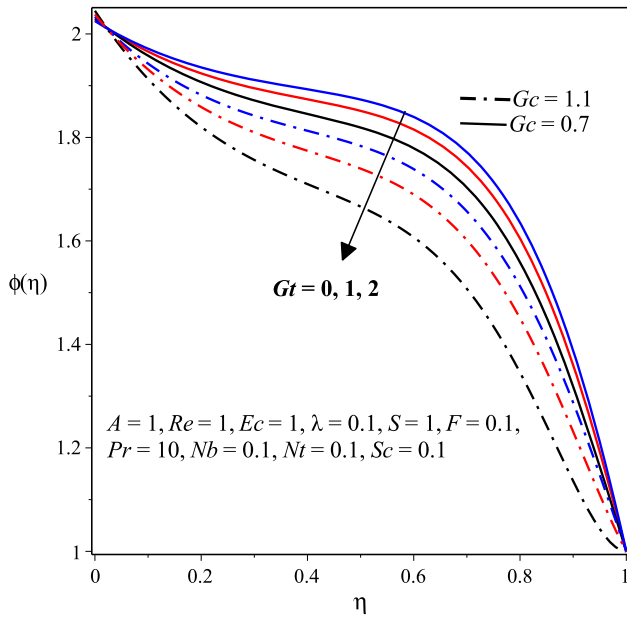


Fig. 7 Effects of Gt and Gc on concentration profile

Ec increases, both the fluid velocity and temperature also increase. This result is similar to the one obtained in the papers [35, 36]. Physically, the Eckert number Ec expresses the relationship between the flow boundary layer enthalpy difference and its kinetic energy which results in more heat to produce, and hence, Ec characterizes the viscous heating within the flow. Therefore, as the magnitude of Ec rises, the viscous heating will be enhanced within the flow resulting in the fluid temperature increment which in turn increases the fluid velocity. Figure 10(b) displays the opposite phenomena for the concentration profile.

Figures 11(a), 12 and 13(b) depict the effects of the porous medium parameters S and F on the velocity, temperature and concentration profiles. Figure 11(a) and 11(b) portrays that both the velocity and temperature profiles decrease significantly as the porous medium shape parameter S increases. From the literature, the studies in [35, 37] reported similar results. The reason behind this result is the fact that as the value of S increases, the porous medium permeability decreases which should naturally dampen the fluid flow and thus the observed decline in the magnitude of fluid velocity which also results in the decrement of viscous heating and in turn decreases the magnitude of fluid temperature. On the contrary, Fig. 13(a) reveals that as the porous medium shape parameter S increases, the concentration profile increases.

In Fig. 12(a) and 12(b), it is observed that the fluid velocity and temperature profiles decrease with increasing values of the Forchheimer number F which is also known as inertial resistance parameter. Physically, large values of F imply the stronger resistant inertial force in the direction normal to the fluid flow which is due to the intensive dimensionless drag force coefficient b since $F = \frac{ba}{\rho\sqrt{K}}$. For higher values of b, stronger resistivity inertial force is effective within the fluid flow so that the velocity becomes smaller and consequently the fluid temperature decreases. From Fig. 13(b), we can see that the Forchheimer number F shows the opposite effect on the concentration profile.

Figure 14(a) and 14(b) is double graphs that display the effects of the Prandtl number Pr and the thermophoresis parameter Nt on the velocity and temperature profiles. Accordingly, the larger values of Pr lead to a significant decrease in the temperature profile since higher values of

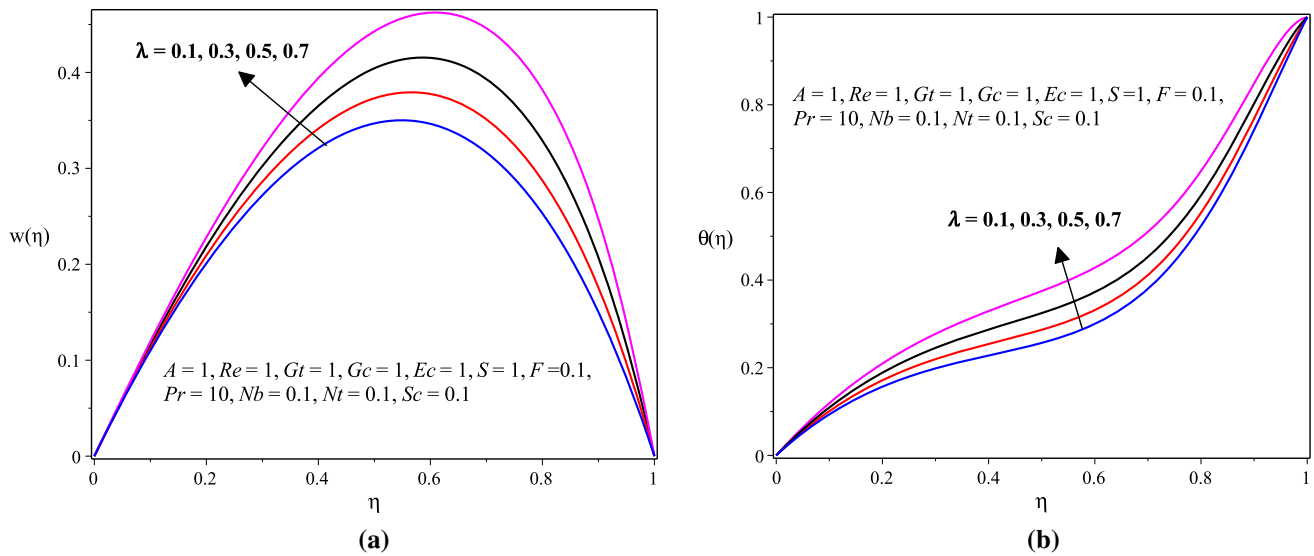


Fig. 8 (a) Velocity and (b) temperature profiles with varying λ

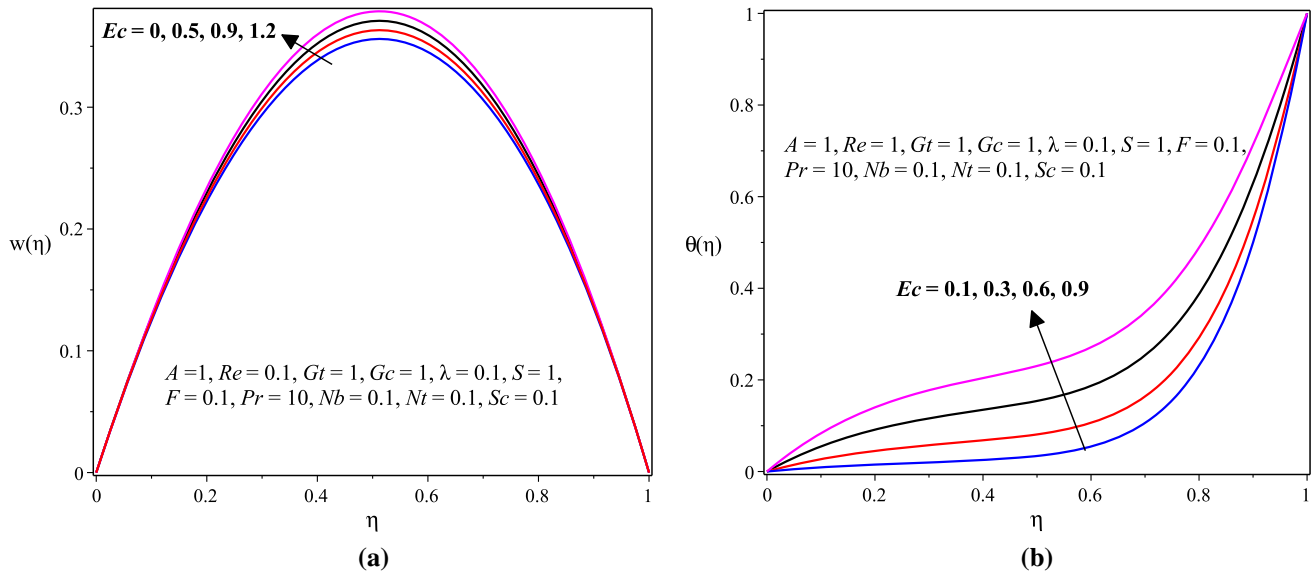


Fig. 9 (a) Velocity and (b) temperature profiles with varying Ec

Pr correspond to low thermal diffusivity of the fluid (Pr and thermal diffusivity have inverse relationship) which reduces the rate at which heat is transported from the heated micro-channel walls into the fluid that was initially at zero temperature. Hence, as observed in Fig. 14(b) the fluid temperature decreases as the value of Pr increases which in turn decreases the fluid velocity profile as shown in Fig. 14(a). This result is similar to the one obtained by [36, 37] and [38], but the opposite was observed in [35]. On the other hand, thermophoresis is a mechanism in which small particles are pulled away from hot surface to cold one, and thus, Fig. 14(a) and 14(b) declares that as the value of Nt enhances, both the velocity and temperature profiles also enhance. The reason behind this argument is

that an enhancement in Nt yields a stronger thermophoretic force which allows deeper migration of nanoparticles from hot surface to cold fluid resulting in higher fluid temperature which in turn results in higher fluid velocity. Figure 15(a) shows that the concentration profile increases with both the Prandtl number Pr and the thermophoresis parameter Nt .

Figure 15(b) is also a double graph that displays the effects of Sc and Nb on the concentration profile. It shows that the concentration profile increases with the Schmidt number Sc . Physically, larger values of Schmidt number Sc indicate less mass diffusion which causes the concentration of nanoparticles to remain larger in the fluid. On the other hand, the Brownian motion is an arbitrary disorganized

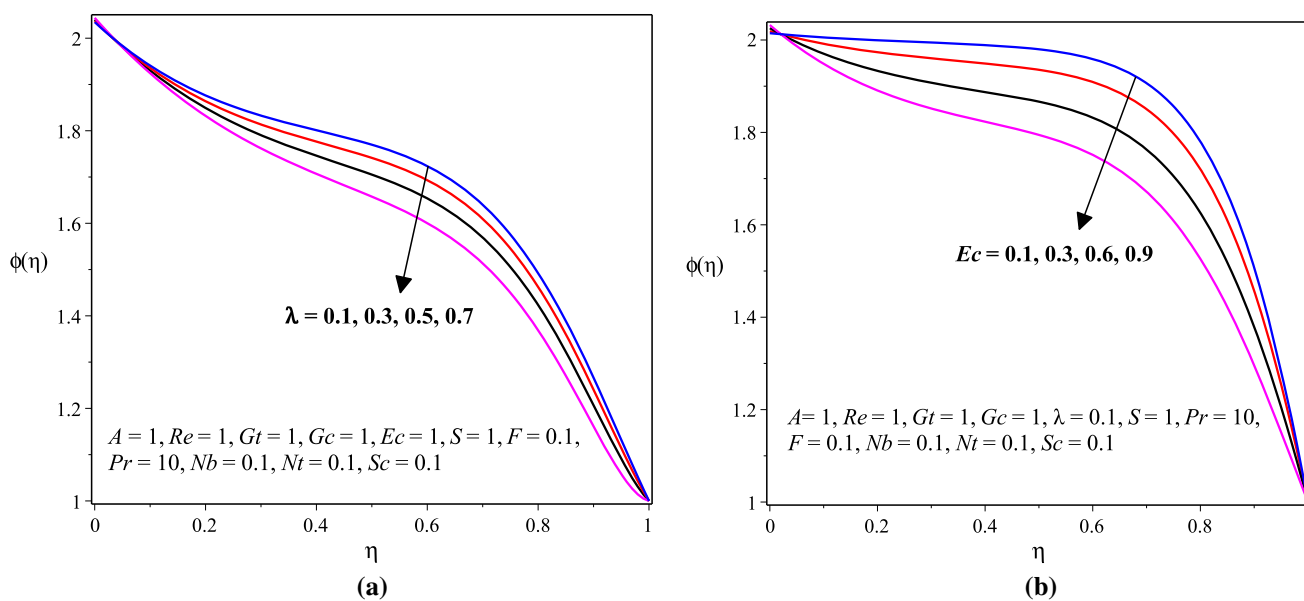


Fig. 10 (a) Effect of λ on concentration profile and (b) effect of Ec on concentration profile

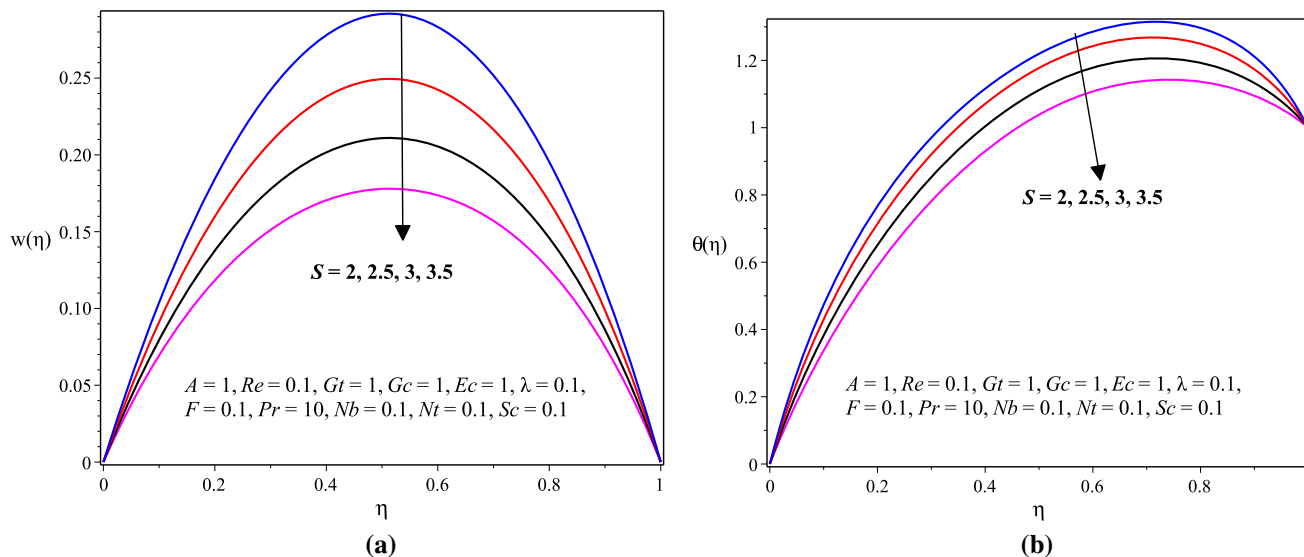


Fig. 11 (a) Velocity and (b) temperature profiles with varying S

motion of nanoparticles dispersed in the base fluid resulting from their collision with moving molecules of the base fluid. Consequently, the concentration profile shows a decreasing behavior with increasing values of the Brownian diffusion parameter Nb as shown in Fig. 15(b). The argument behind this result is that when the magnitudes of Nb increase, the random motion and also collision of the nanoparticles in the fluid increase which reduce the concentration of the nanoparticles in the fluid.

5.3. The wall shear stress, wall heat transfer and mass transfer rates

This subsection comprises the effects of flow parameters on the wall shear stress, wall heat and mass transfer rates. Indeed, the graphical results that are illustrated in this subsection for the skin friction coefficient C_f , the Nusselt number Nu and the Sherwood number Sh are plotted for large time, say $\tau \geq 2$ (steady state), and thus, the results obtained may not be affected by time increasing for all parameters values as a consequence of the results obtained in Sect. 5.1.

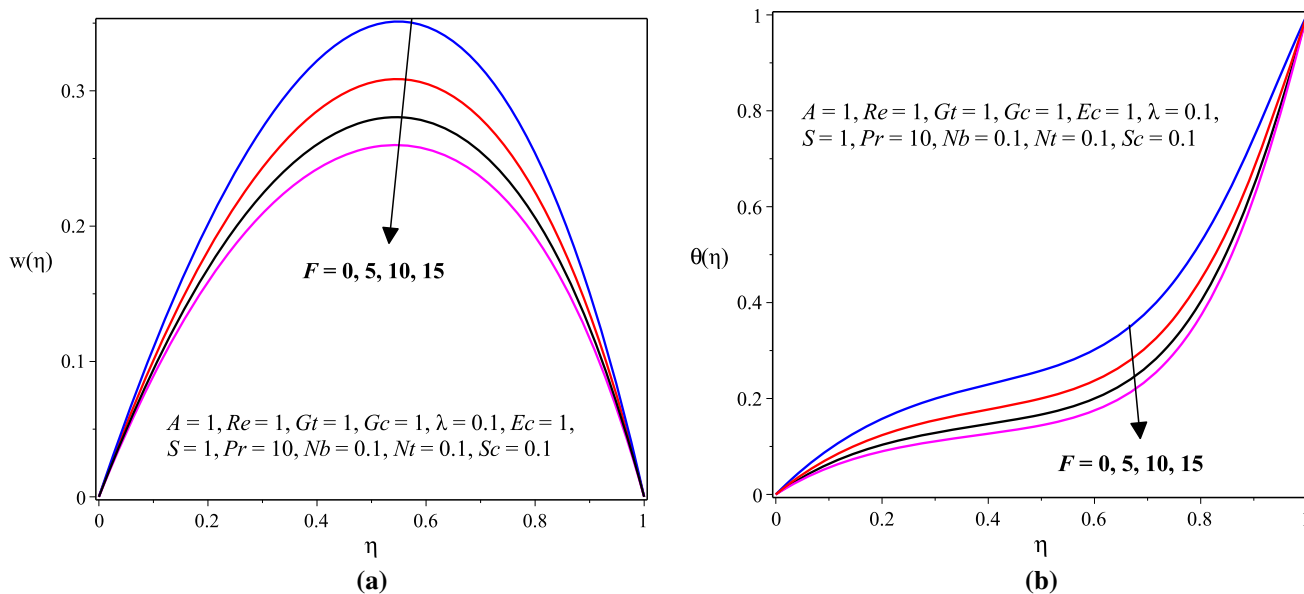


Fig. 12 (a) Velocity and (b) temperature profiles with varying F

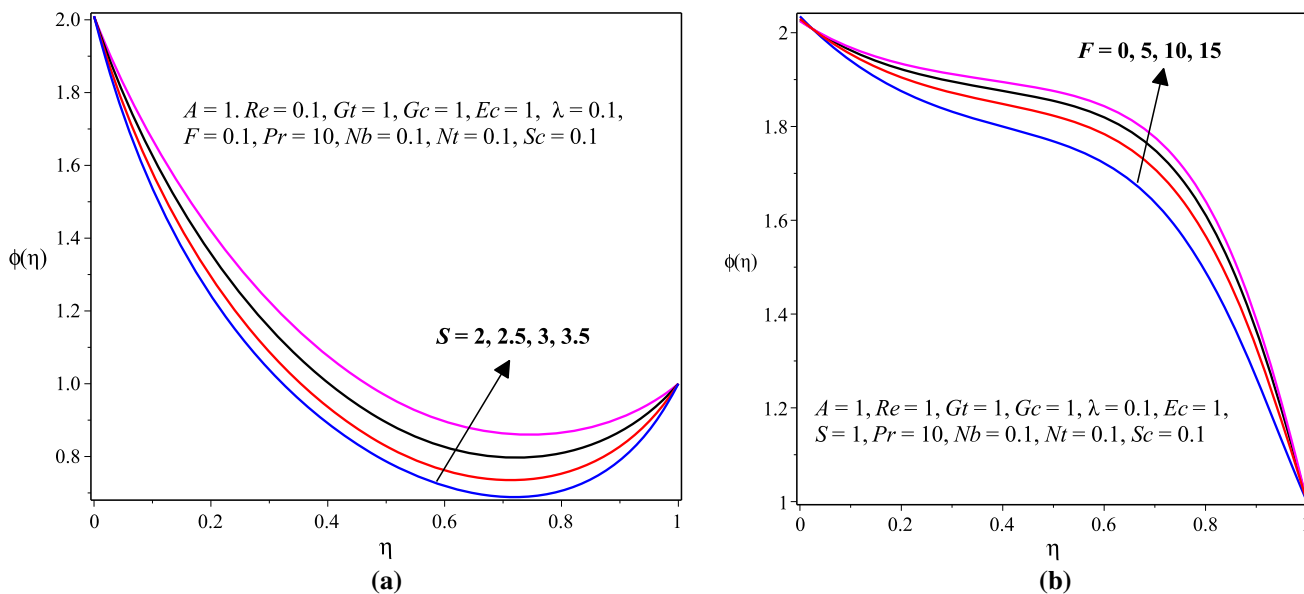


Fig. 13 (a) Effect of S on concentration profile and (b) effect of F on concentration profile

5.3.1. The wall shear stress: skin friction coefficient

The effects of pertinent parameters on the wall shear stress at the left wall $\eta = 0$ and at the right wall $\eta = 1$ are illustrated in Figs. 16(a), 17, 18 and 19(b). Consequently, from these graphs it can be observed that the wall shear stress, coefficient of skin friction C_f (at both left and right walls), shows an increasing behavior with increasing values of the Eckert number Ec and the thermal Grashof number Gt for varying scaled values of the suction/injection Reynolds number Re . The results in the works of [35, 36] are similar to the outcomes of our paper. The

pressure gradient parameter A , the Schmidt number Sc and the Prandtl number Pr also show an increasing effect on C_f (at both left and right walls) for varying scaled values of the suction/injection Reynolds number Re . However, the Forchheimer number F and the porous medium shape parameter S have a decreasing effect on C_f at both walls of the micro-channel. In addition, C_f increases as the values of the variable viscosity parameter λ increase at the left wall of the micro-channel $\eta = 0$ (see Fig. 19(a)), whereas C_f decreases with increasing values of the variable viscosity parameter λ at the right wall $\eta = 1$ (see Fig. 19(b)).

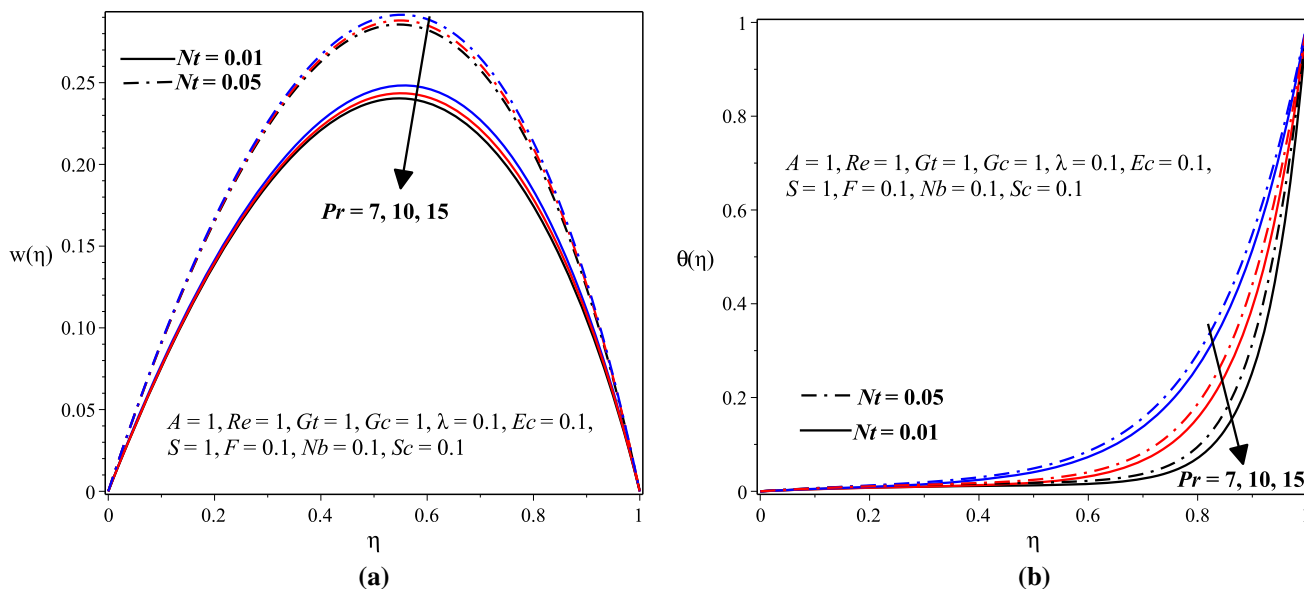


Fig. 14 (a) Velocity and (b) temperature profiles with varying Pr and Nt

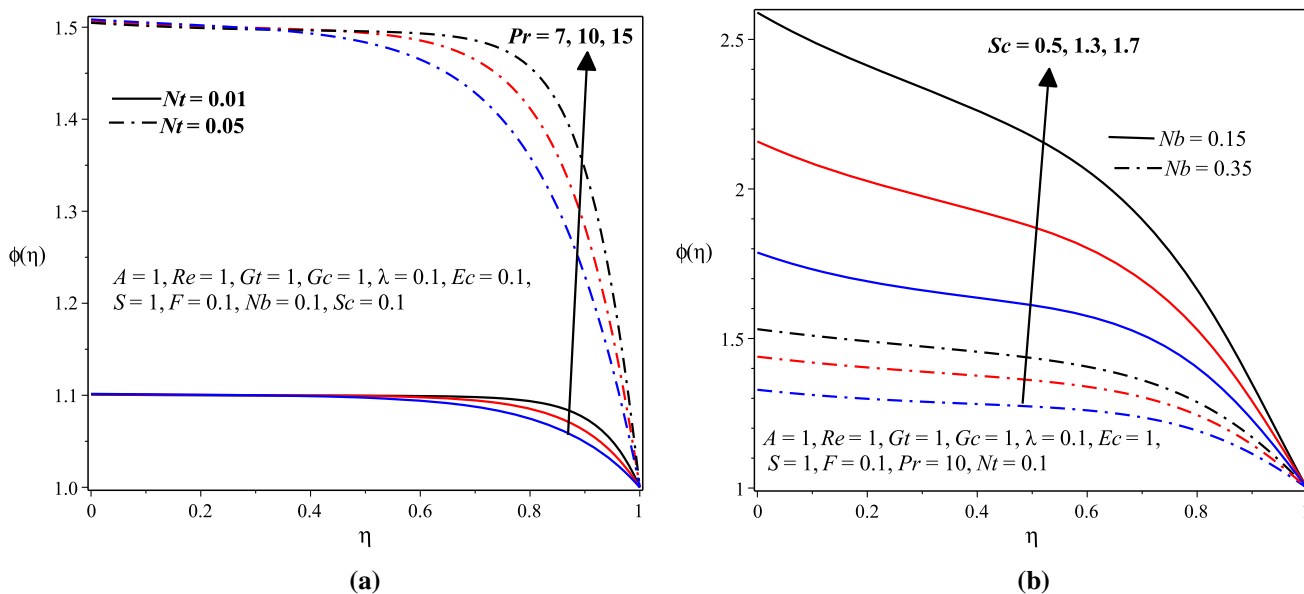


Fig. 15 (a) Effects of Pr and Nt on concentration profile and (b) effects of Sc and Nb on concentration profile

5.3.2. The wall heat transfer rate: Nusselt number

The effects of prominent governing flow parameters on the wall heat transfer rate at the left wall $\eta = 0$ and at the right wall $\eta = 1$ are portrayed in Figs. 20(a), 21, 22 and 23(b). Accordingly, from these graphs we can see that the wall heat transfer rate, the Nusselt number Nu , at both left and right walls shows an increasing behavior with increasing values of the variable viscosity parameter λ and the thermal Grashof number Gt for varying scaled values of the suction/injection Reynolds number Re . This result is similar to the one obtained by [35]. Likewise, Nu at both left and

right walls shows an increasing behavior with increasing values of the pressure gradient parameter A , the Schmidt number Sc and the Prandtl number Pr for varying scaled values of the suction/injection Reynolds number Re . Nevertheless, the Forchheimer number F and the porous medium shape parameter S have a decreasing effect on Nu at both walls of the micro-channel. As presented in Fig. 21(a), the Nusselt number Nu increases as values of the Eckert number Ec increase at the left wall of the micro-channel $\eta = 0$, but Fig. 21(a) reveals that Nu decreases with increasing values of the Eckert number Ec at the right wall $\eta = 1$.

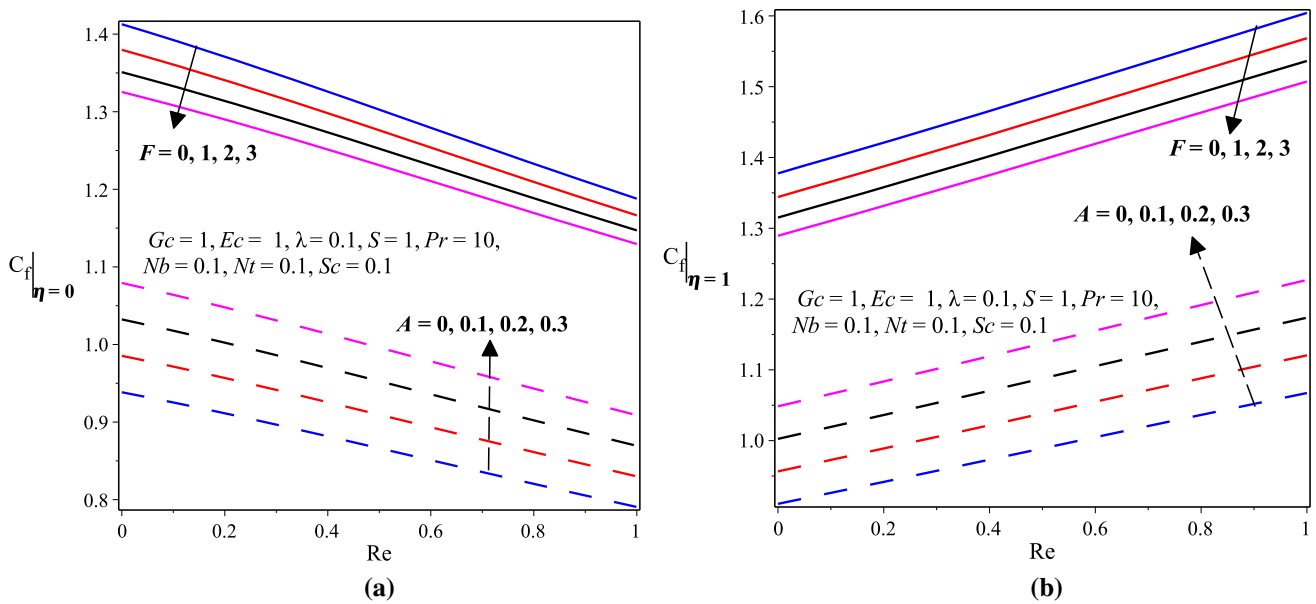


Fig. 16 (a) Skin friction at $\eta = 0$ and (b) skin friction at $\eta = 1$ with varying A, F and Re

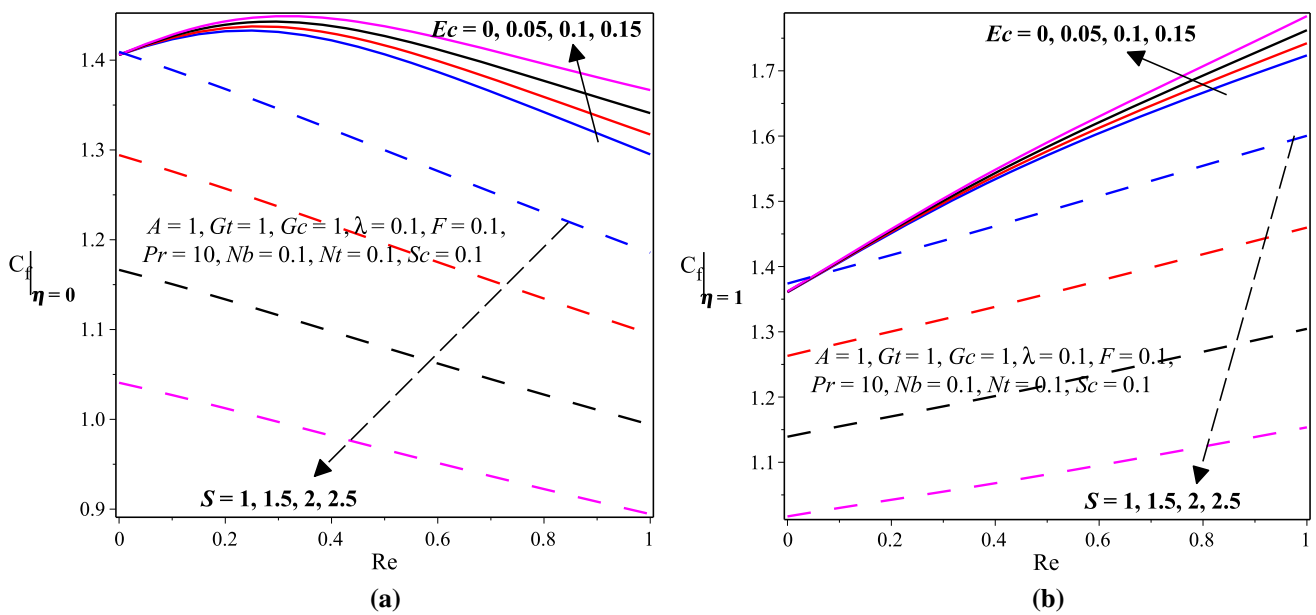


Fig. 17 (a) Skin friction at $\eta = 0$ and (b) skin friction at $\eta = 1$ with varying S, Ec and Re

5.3.3. The wall mass transfer rate: Sherwood number

The effects of governing flow parameters on the wall mass transfer rate at the left wall $\eta = 0$ and at the right wall $\eta = 1$ are given in Figs. 24(a), 25, 26 and 27(b). As a result, these graphs depict that the wall mass transfer rate, Sherwood number Sh , at both left and right walls shows an increasing trend with increasing values of the pressure gradient parameter A , the variable viscosity parameter λ , the thermal Grashof number Gt , the Schmidt number Sc and the Prandtl number Pr for varying scaled values of the

suction/injection Reynolds number Re . Nonetheless, the Forchheimer number F and the porous medium shape parameter S have a decreasing effect on Sh at both walls of the micro-channel. From Fig. 25(a), it is noticed that Sh increases as values of the Eckert number Ec increase at the left wall of the micro-channel $\eta = 0$, while Fig. 25(b) shows that Sh decreases with increasing values of the Eckert number Ec at the right wall $\eta = 1$.

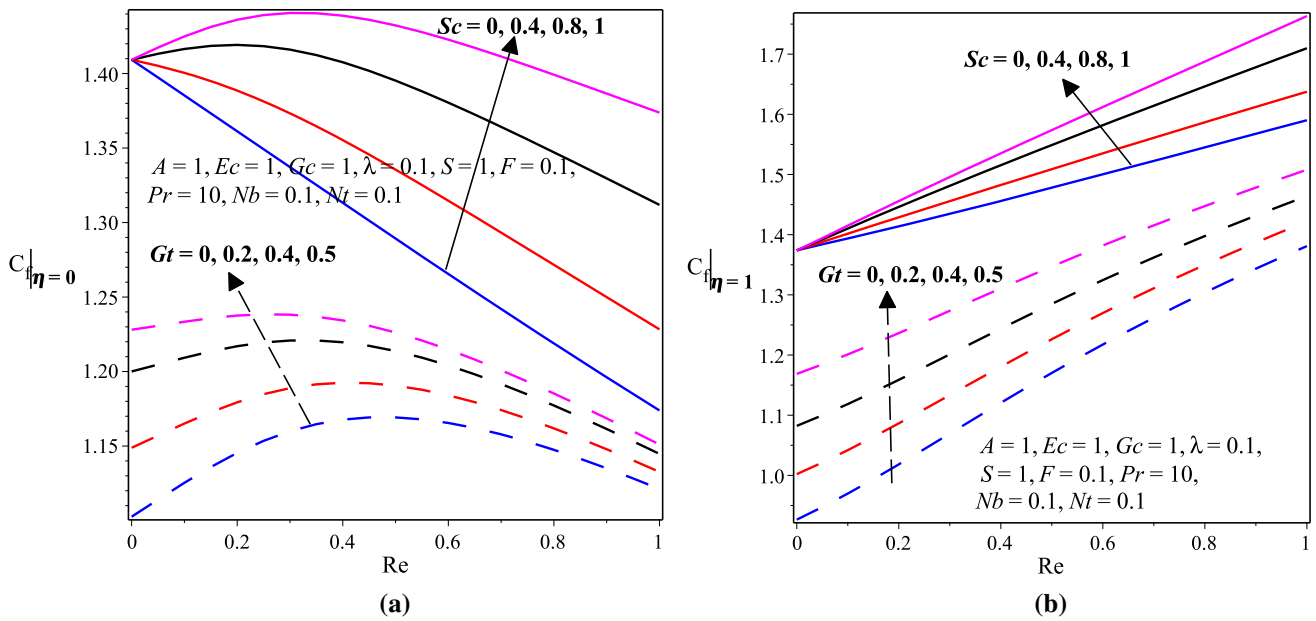


Fig. 18 (a) Skin friction at $\eta = 0$ and (b) skin friction at $\eta = 1$ with varying Gt, Sc and Re

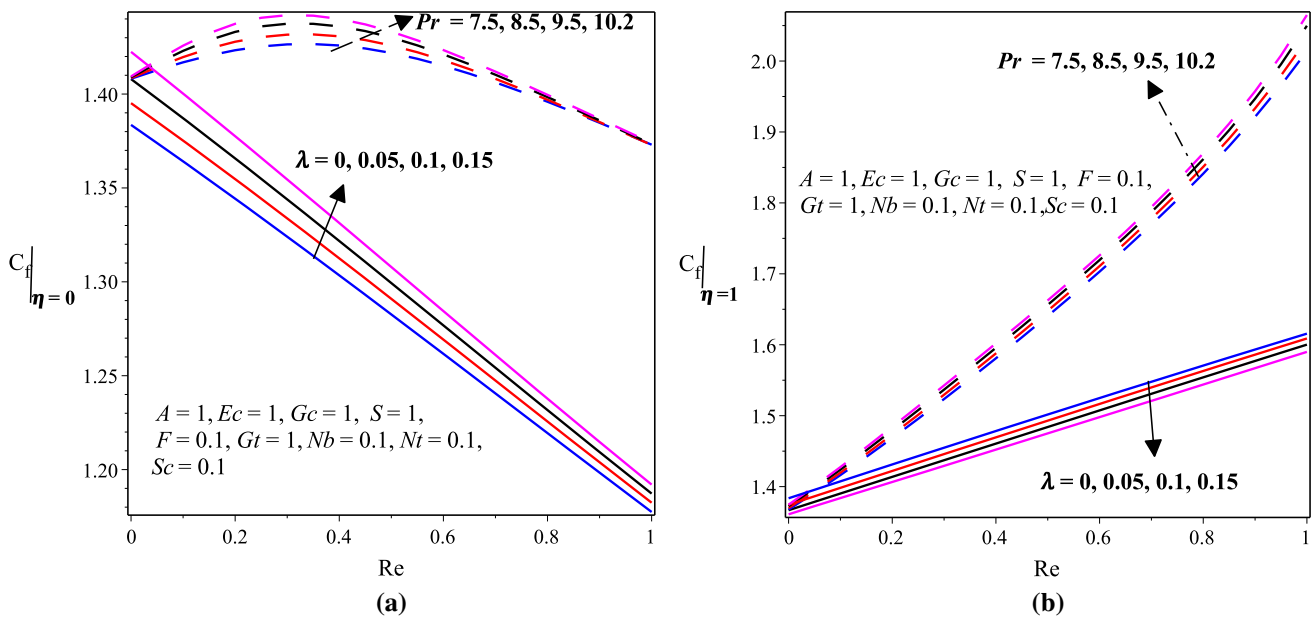


Fig. 19 (a) Skin friction at $\eta = 0$ and (b) skin friction at $\eta = 1$ with varying λ, Pr and Re

6. Conclusions

In the present study, we investigated the flow and heat transfer characteristics of unsteady mixed convection flow of variable viscosity nanofluid in a micro-channel filed with a saturated porous medium under the influences of axial pressure gradient, suction/injection as well as thermal and solutal buoyancy forces. The governing highly non-linear partial differential equations corresponding to the momentum, energy and concentration fields were

formulated and solved numerically by utilizing the semi-discretization finite difference method. Therefore, based on the above results we pointed out the following conclusions.

- Both the velocity and temperature profiles show an increasing behavior with increasing values of the pressure gradient parameter A , the variable viscosity parameter λ , the Eckert number Ec , the thermal Grashof number Gt , the solutal Grashof number Gc and the thermophoresis parameter Nt .

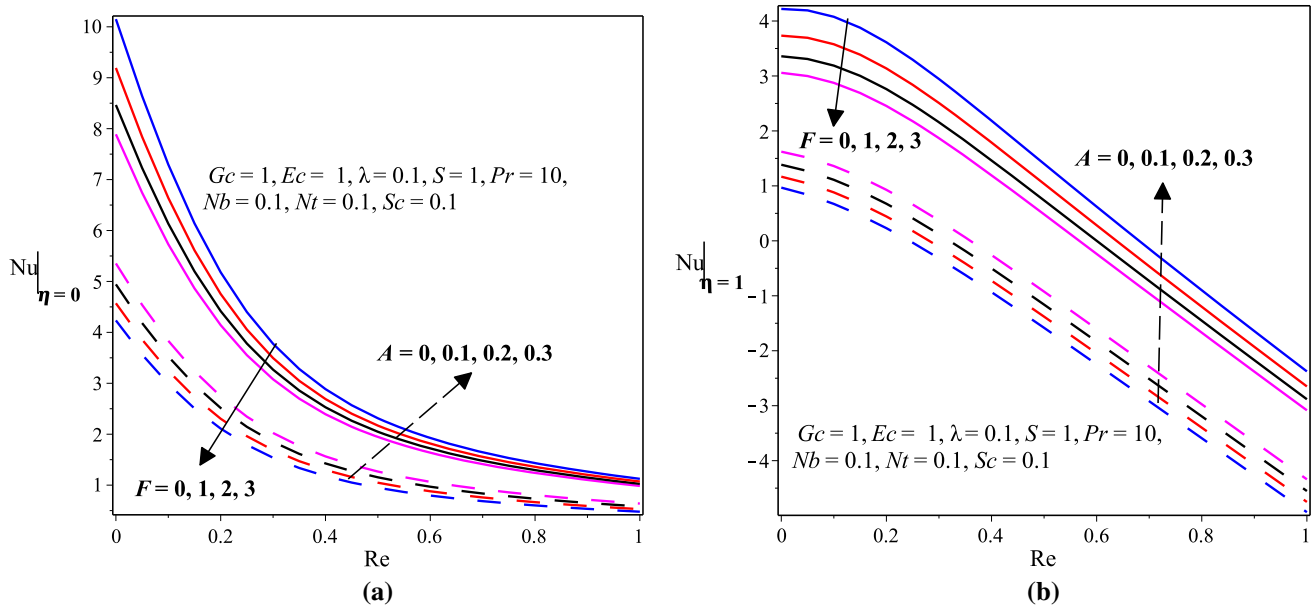


Fig. 20 (a) Nusselt number at $\eta = 0$ and (b) Nusselt number at $\eta = 1$ with varying A , F and Re

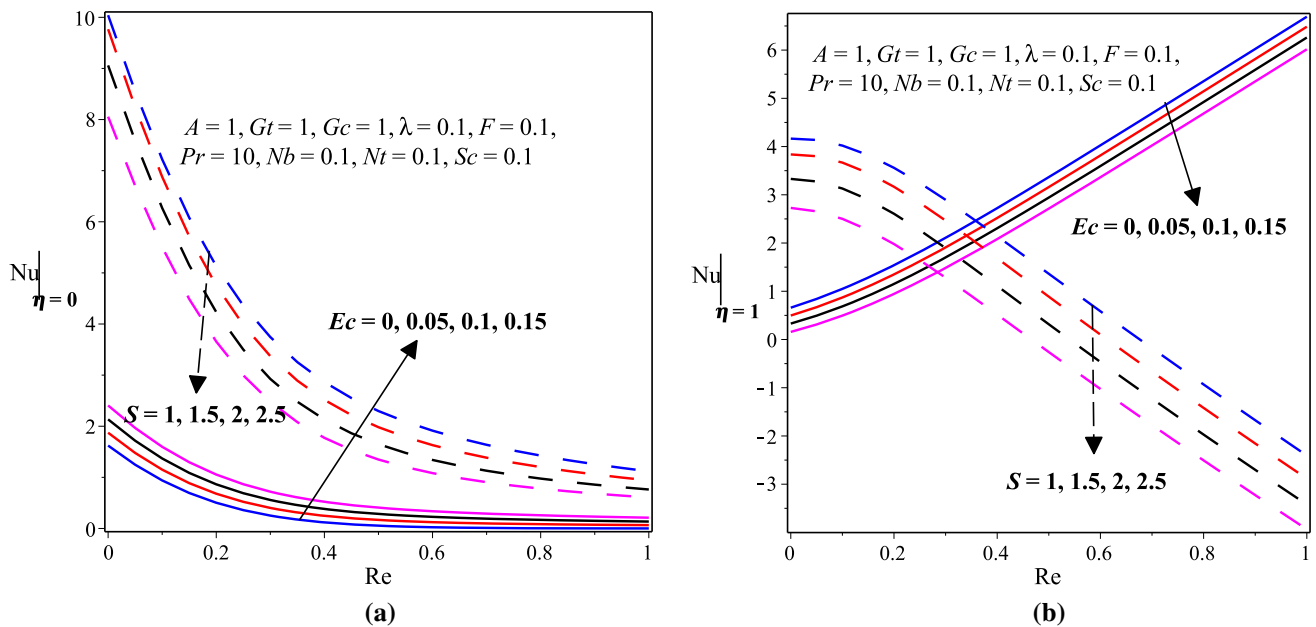


Fig. 21 (a) Nusselt number at $\eta = 0$ and (b) Nusselt number at $\eta = 1$ with varying S , Ec and Re

- The concentration profile indicates an increasing trend with increasing values of the suction injection Reynolds number Re , the porous medium shape parameter S , the Forchheimer number F , the Prandtl number Pr , the Schmidt number Sc and the thermophoresis parameter Nt .
- The skin friction coefficient C_f is large for higher values of the pressure gradient parameter A , the Eckert number Ec , the thermal Grashof number Gt , the Schmidt number Sc and the Prandtl number Pr on both sides of the micro-channel walls.
- Both the Nusselt number Nu and the Sherwood number Sh show an increasing pattern with an increasing values of the pressure gradient parameter A , the variable viscosity parameter λ , the thermal Grashof number Gt , the Schmidt number Sc and the Prandtl number Pr on both sides of the micro-channel walls.

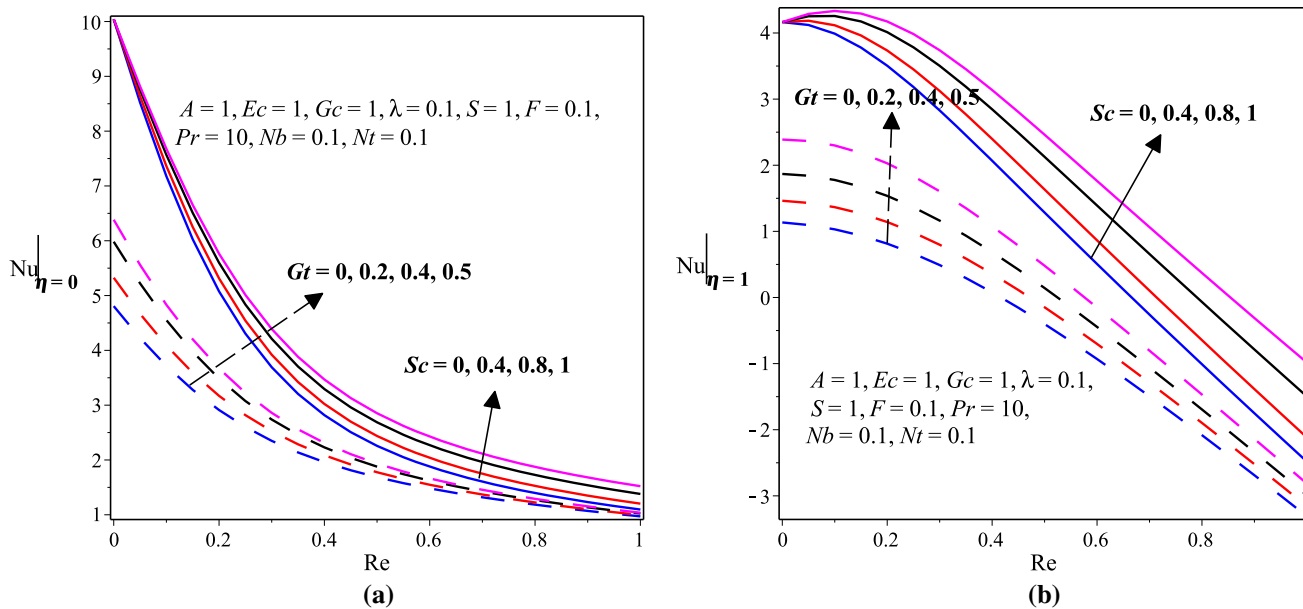


Fig. 22 (a) Nusselt number at $\eta = 0$ and (b) Nusselt number at $\eta = 1$ with varying Gt, Sc and Re

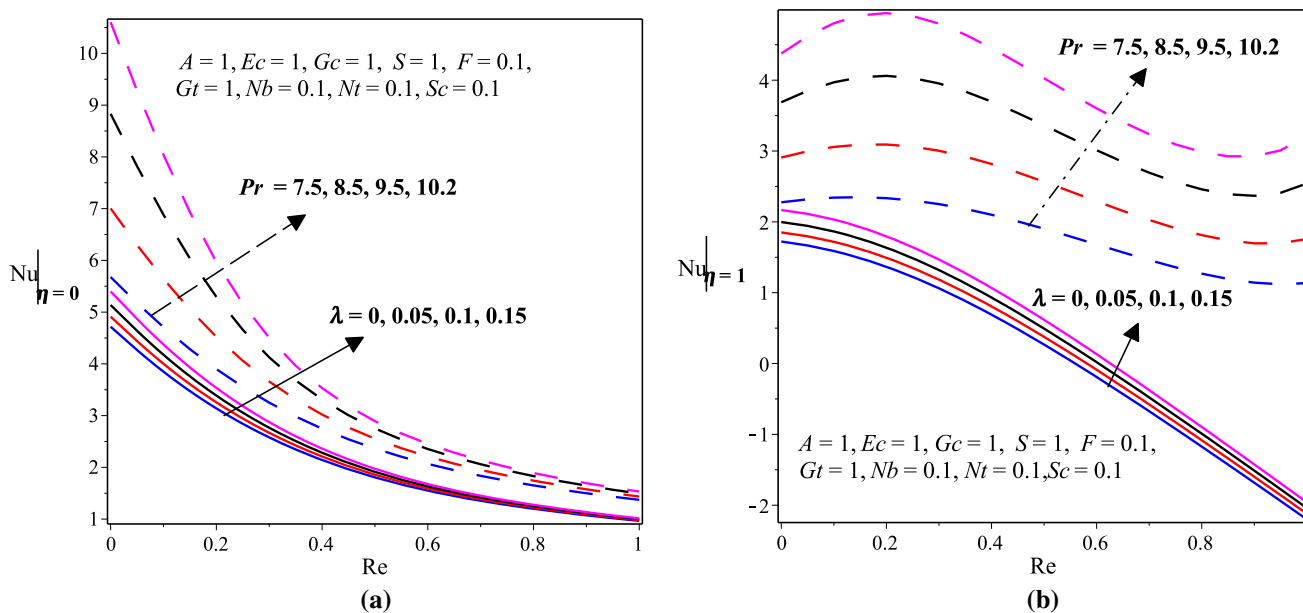


Fig. 23 (a) Nusselt number at $\eta = 0$ and (b) Nusselt number at $\eta = 1$ with varying λ, Pr and Re

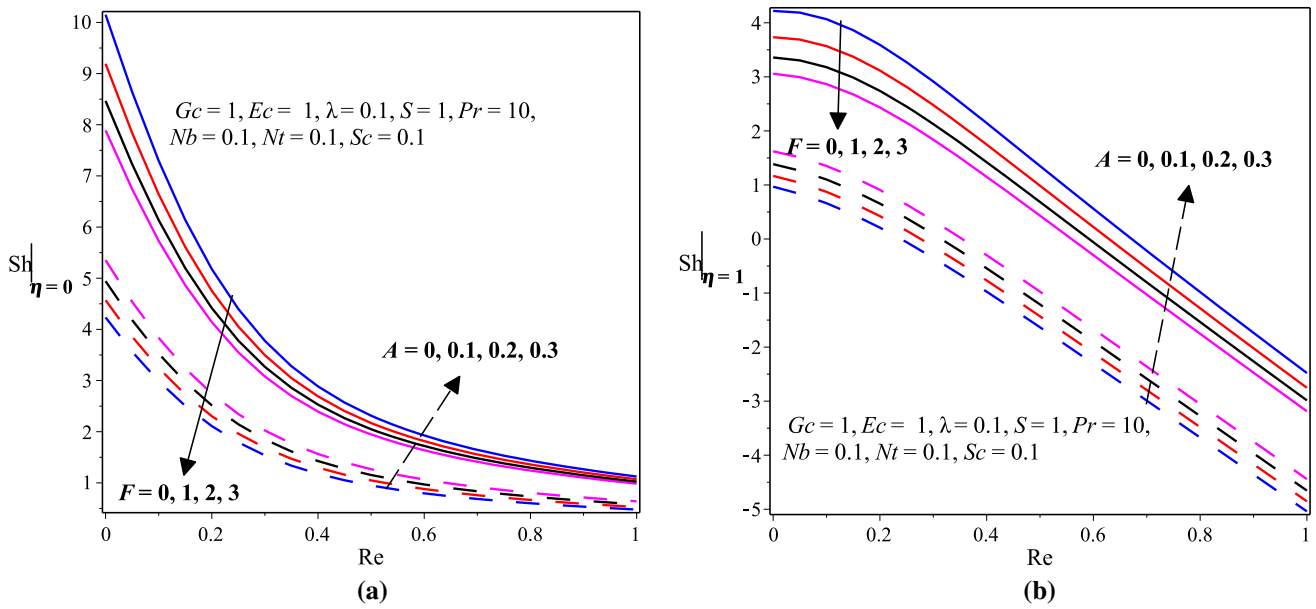


Fig. 24 (a) Sherwood number at $\eta = 0$ and (b) Sherwood number at $\eta = 1$ with varying A, F and Re

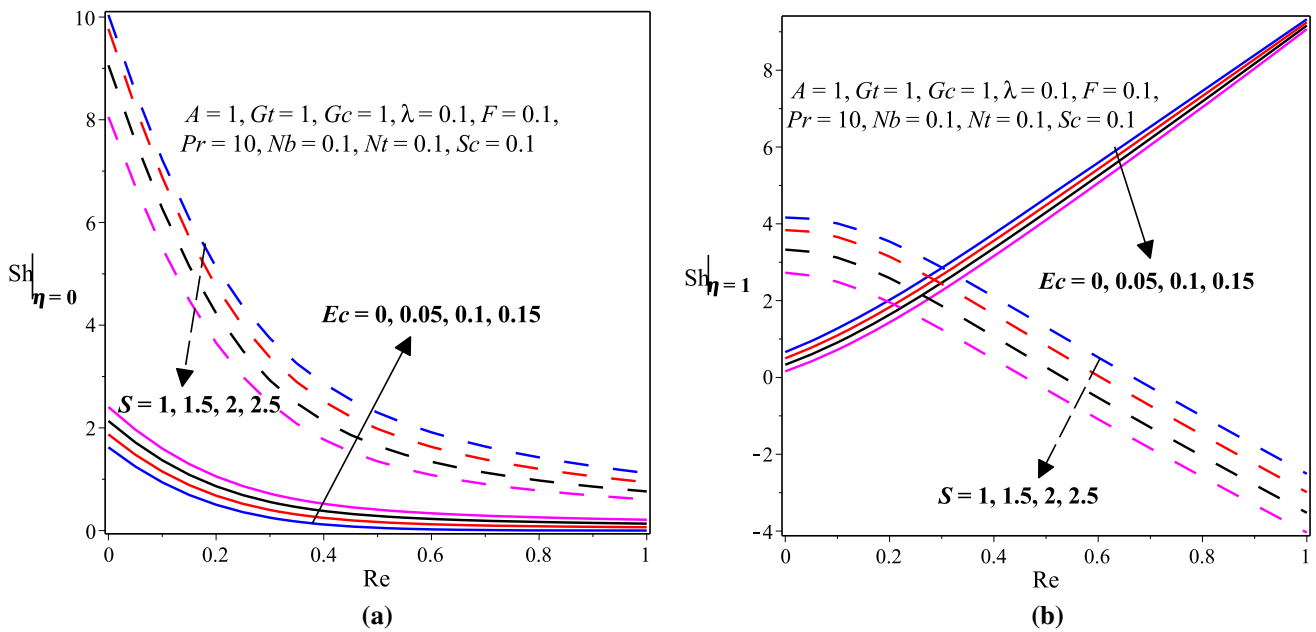


Fig. 25 (a) Sherwood number at $\eta = 0$ and (b) Sherwood number at $\eta = 1$ with varying S, Ec and Re

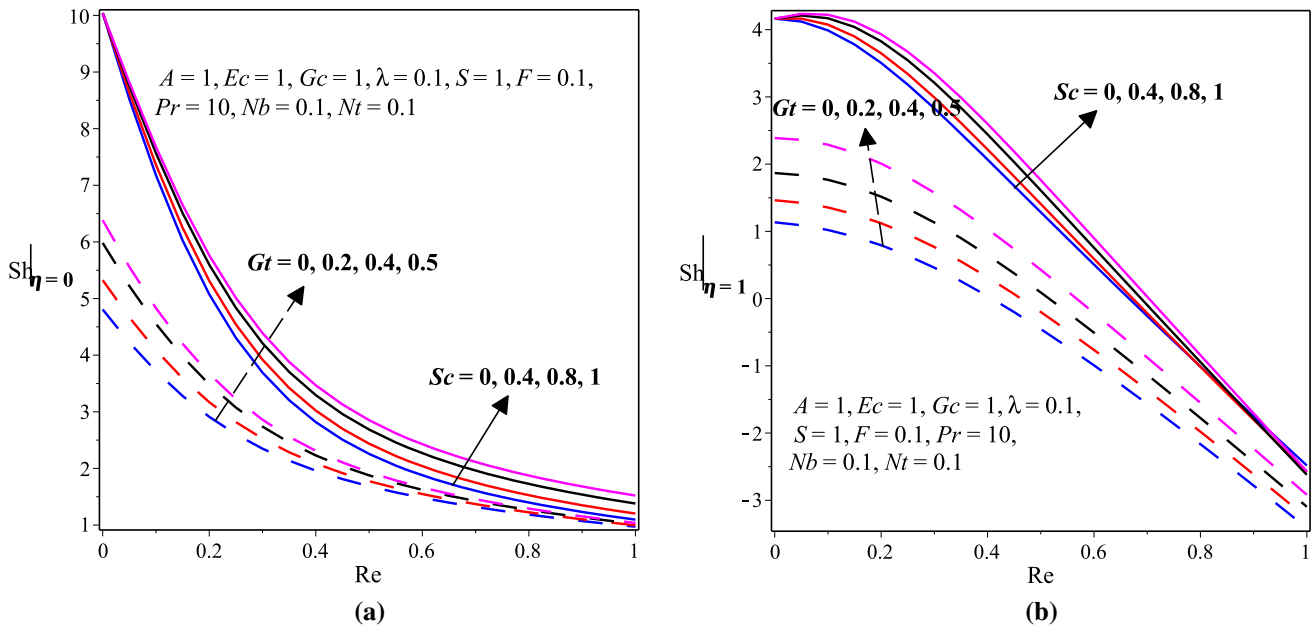


Fig. 26 (a) Sherwood number at $\eta = 0$ and (b) Sherwood number at $\eta = 1$ with varying Gt , Sc and Re

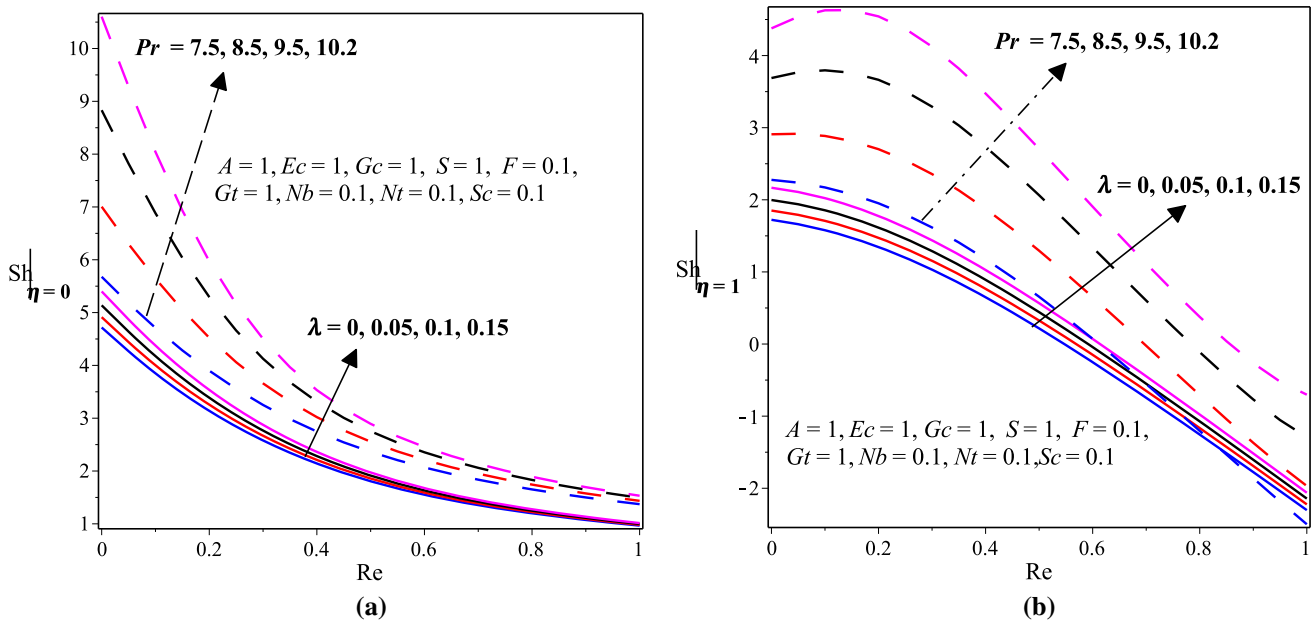


Fig. 27 (a) Sherwood number at $\eta = 0$ and (b) Sherwood number at $\eta = 1$ with varying λ , Pr and Re

Acknowledgements The corresponding author is profoundly grateful to the financial support of Adama Science and Technology University (Grant No. ASTU/SP-R/073/20).

References

- [1] D D Ganji and A Malvandi *Heat Transfer Enhancement Using Nanofluid Flow in Microchannels: Simulation of Heat and Mass Transfer* (San Diego, USA: Elsevier Inc.) (2016)
- [2] S G Kandlikar, S Garimella, D Li, S Colin and M R King *Heat Transfer and Fluid Flow in Minichannels and Microchannels* (San Diego, USA: Elsevier Ltd.) (2006)
- [3] D B Tuckerman and R F Pease *IEEE Electron Device Lett.* **2** 126 (1981)

- [4] S K Rai, R Sharma, M Saifi, R Tyagi, D Singh and H Gupta *Int. J. Appl. Eng. Res.* **13** 64 (2018)
- [5] M Jahangiri, R Y Farsani and A A Shamsabadi *J. Mech. Eng. Technol.* **10** 2 (2018)
- [6] C A Saleel, A Algahtani, I A Badruddin, T M Y Khan, S Kamangar and M A H Abdelmohimen *J. Appl. Fluid. Mech.* **13** 429 (2019)
- [7] K V Reddy, O D Makinde and M G Reddy *Indian J. Phys.* **92** 1439 (2018)
- [8] M Kmiołek and A Kucab-Pietal *Bull. Pol. Acad. Tech. Sci.* **66** 2 (2018)
- [9] A Ahadi, S Antoun, M Z Saghir and J Swift *Energy Storage* **1** e37 (2019)
- [10] M Venkateswarlu, M Prameela and O D Makinde *J. Nanofluids* **8** 1506 (2019)
- [11] J Moon, J R Pacheco and A Pacheco-Vega *Proceedings of the 4th World Congress on Momentum, Heat and Mass Transfer (MHMT'19)* (Rome Italy) ENFHT 120 (2019)
- [12] A Dewan and P Srivastava *J. Therm. Sci.* **24** 203 (2015)
- [13] R Kumar, M Islam and M M Hasan *Int. J. Adv. Mech. Eng.* **4** 115 (2014)
- [14] S U S Choi *ASME Fluids Eng. Div.* **231** 99 (1995)
- [15] M Sheikholeslami, M Jafaryar, E Abohamzeh, A Shafee and H Babazadeh *Sustain. Energy Technol. Assess.* **39** 100727 (2020)
- [16] A Jedi et al. *Colloids Interfaces* **4** 3 (2020)
- [17] K R V Subramanian, T N Rao and A Balakrishnan (eds) *Nanofluids and Their Engineering Applications* (New York, USA: Taylor & Francis Group, LLC CRC Press) (2020)
- [18] K V Reddy, M G Reddy and O D Makinde *J. Nanofluids* **8** 349 (2019)
- [19] O Z Sharaf, A N Al-Khateeb, D C Kyritsis and E Abu-Nada *J. Fluid Mech.* **878** 62 (2019)
- [20] H Xu, H Huang, X H Xu, Q Sun *Int. J. Numer. Methods Heat Fluid Flow* (2019)
- [21] A K Patel, S Bhuvad and S P S Rajput *Int. J. Innov. Technol. Explor. Eng.* **9** 5230 (2019)
- [22] M D K Niazi and H Xu *Appl. Math. Mech.* **41** 83 (2019)
- [23] M I Shahrestani, A Maleki, M S Shadloo and I Tlili *Symmetry* **12** 120 (2020)
- [24] Y Mahmoudi, K Hooman and K Vafai (eds) *Convective Heat Transfer in Porous Media* (New York, USA: Taylor & Francis Group, LLC CRC Press) (2020)
- [25] A A A Al-Rashed, G A Sheikhzadeh, A Aghaei, F Monfared, A Shahsavari and M Afrand *J. Therm. Anal. Calorim.* (2019)
- [26] M Muthamilselvan and S S Ureshkumar *J. Theor. Appl. Mech.* **48** 50 (2018)
- [27] S Whitaker (1986) *Transp. Porous Media* **1** 3 (1986)
- [28] M Venkateswarlu, O D Makinde and D V Lakshmi *J. Nanofluids* **8** 1010 (2019)
- [29] C S Delisle, C A Welsford and M Z Saghir *J. Therm. Anal. Calorim.* (2019)
- [30] N S Shashikumar, B C Prasannakumara, B J Gireesha and O D Makinde *Diffus. Found.* **16** 120 (2018)
- [31] B J Gireesha, C T Srinivasa, N S Shashikumar, M Macha, J K Singh and B Mahanthesh *J. Process Mech. Eng.* **0** 1 (2019)
- [32] B Aina and P B Malgwi *Nonlinear Eng.* **8** 755 (2019)
- [33] J Buongiorno *ASME J. Heat Transf.* **128** 240 (2006)
- [34] O D Makinde *Defect Diffus. Forum* **387** 182 (2018)
- [35] L Rundora and O D Makinde *J. Porous Media* **21** 721 (2018)
- [36] O D Makinde, Z H Khan, R Ahmad, Rizwan Ul Haq and W A Khan *Int. J. Appl. Comput. Math.* **5** 59 (2019)
- [37] L Rundora and O D Makinde *Appl. Math. Inf. Sci.* **12** 483 (2018)
- [38] S Sarkar, M F Endalew and O D Makinde *J. Appl. Comput. Mech.* **5** 763 (2019)

Publisher's Note Springer Nature remains neutral with regard to jurisdictional claims in published maps and institutional affiliations.